
Five Pediatric Head and Brain Mathematical Models for Use in Internal Dosimetry

Lionel G. Bouchet and Wesley E. Bolch

Department of Nuclear and Radiological Engineering, University of Florida, Gainesville, Florida

Mathematical models of the head and brain currently used in pediatric neuroimaging dosimetry lack the anatomic detail needed to provide the necessary physical data for suborgan brain dosimetry. To overcome this limitation, the Medical Internal Radiation Dose (MIRD) Committee of the Society of Nuclear Medicine recently adopted a detailed dosimetric model of the head and brain for the adult. **Methods:** New head and brain models have been developed for a newborn, 1, 5, 10 and 15 y old for use in internal dosimetry. These models are based on the MIRD adult head and brain model and on published head and brain dimensions. They contain the same eight brain subregions and the same head regions as the adult model. These new models were coupled with the Monte Carlo transport code EGS4, and absorbed fractions of energy were calculated for 14 sources of monoenergetic photons and electrons in the energy range of 10 keV–4 MeV. These absorbed fractions were then used along with radionuclide decay data to generate S values for all ages for ^{99m}Tc , considering 12 source and 15 target regions. **Results:** Explicit transport of positrons was also considered with separation of the annihilation photons component to the absorbed fraction of energy in the calculation of S values for positron-emitting radionuclides. No statistically significant differences were found when S values were calculated for positron-emitting radionuclides under explicit consideration of the annihilation event compared with the traditional assumption of a uniform distribution of 0.511-MeV photons. **Conclusion:** The need for electron transport within the suborgan brain regions of these pediatric phantoms was reflected by the relatively fast decrease of the self-absorbed fraction within many of the brain subregions, with increasing particle energy. This series of five dosimetric head and brain models will allow more precise dosimetry of radiopharmaceuticals in pediatric nuclear medicine brain procedures.

Key Words: brain dosimetry; suborgan dosimetry; pediatric dosimetry; MIRD schema; S values; ^{99m}Tc

J Nucl Med 1999; 40:1327–1336

To facilitate improvements in the radiation dosimetry of nuclear medicine studies of the brain, the Medical Internal Radiation Dose (MIRD) Committee of the Society of Nuclear Medicine has adopted a new head and brain dosimetric model of the adult (1,2). This model considers eight brain subregions (caudate nuclei, cerebellum, cerebral

cortex, lateral and third ventricles, lentiform nuclei, thalami and white matter) and 11 regions within the head (cranium, cranial cerebrospinal fluid [CSF], eyes, mandible, skin, spinal chord, spinal CSF, spinal skeleton, teeth, thyroid and an upper facial region). The improvements to brain and head dosimetry were illustrated in MIRD Pamphlet No. 15 (2), by a dose calculation using $^{123}\text{I-N-(3-iodopropen-2-yl)-2}\beta\text{-carbomethoxy-3}\beta\text{-(4-chlorophenyl)tropane}$ (IPT), a tropane analog of cocaine that concentrates nonuniformly within the brain (3). It was shown that for this radiopharmaceutical, the absorbed dose to the caudate nuclei and lentiform nuclei was approximately five times the absorbed dose averaged across the total brain, the only dosimetry estimate available from older brain models. The need for improvements in brain dosimetry extends to the studies involving pediatric patients. Existing models that consider the brain as a single elliptical region limit the accuracy and extent of dose calculations.

In pediatric nuclear medicine dosimetry, five anthropomorphic models developed by Cristy and Eckerman are generally used: a newborn, 1, 5, 10 and 15 y old (4,5). These models incorporate simplistic head and brain region geometries. Brain subregions are not outlined, the eyes are not modeled and a distinct neck region is not defined within the head. New pediatric dosimetric models of the head and brain based on the new MIRD adult head and brain model would therefore offer benefits in estimating absorbed dose for pediatric patients undergoing nuclear medicine procedures.

MATERIALS AND METHODS

Five pediatric head and brain models have been developed based on the new MIRD adult head and brain model (2). The shape of each region within these models was kept the same as in the adult model. The equation parameters were adjusted so that the modeled suborgan dimensions were matched to reference values. Figure 1 shows a three-dimensional rendering of the head and brain regions within the dosimetric model. The volumes of the head and brain regions of all regions are given in Table 1. A complete description of the shapes of the head and brain subregions has been published (1,2).

The external dimensions of the head were calculated by keeping the length of the head and neck the same as in the Oak Ridge National Laboratory (ORNL) pediatric models (4,5) and by using breadth and length values published by Krogman (6). The neck radius was derived from circumference values given by Harris et al. (7), and the neck length was derived from the thyroid dimensions (4,5). The center axis of the neck was determined by keeping

Received Aug. 28, 1998; revision accepted Feb. 4, 1999.

For correspondence or reprints contact: Wesley E. Bolch, PhD, Department of Nuclear and Radiological Engineering, University of Florida, Gainesville, FL 32611-8300.

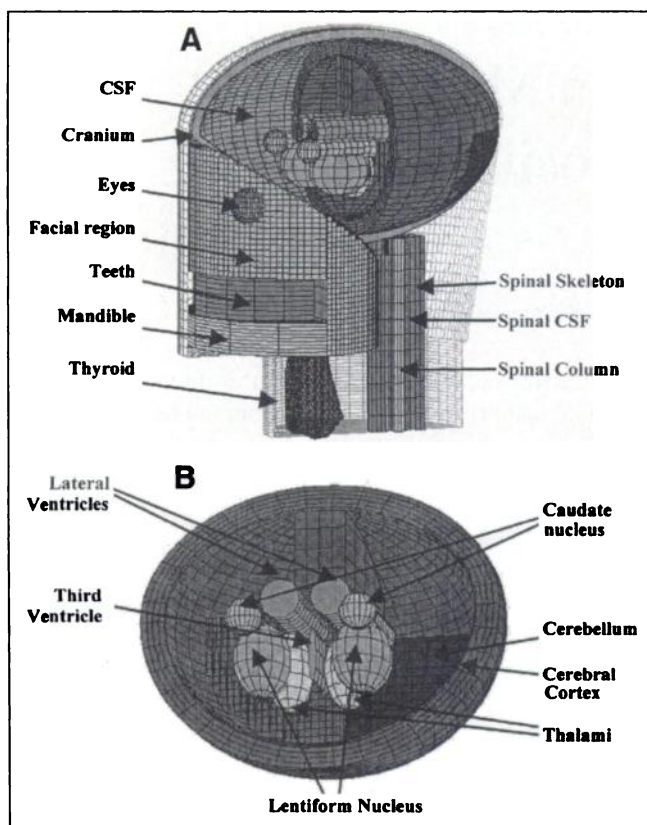


FIGURE 1. Interior features of new MIRD adult head and brain model. (Reprinted with permission from Bouchet LG, Bolch WE, Wessels BW, Weber D. *MIRD Head and Brain Dosimetry*. Reston, VA: Society of Nuclear Medicine; 1999:204.)

constant its relative position compared with the axis of the cylinder of the head. The skin thickness was obtained from data published by Southwood (8) and is the same as in the ORNL pediatric models (4,5).

The cranium was derived in parallel with the cranial CSF (defined later), from the inner dimensions of the head, the outer dimensions of the brain and by keeping the thickness ratios between the cranial CSF and the cranium constant for all ages. The mandible, teeth and upper face regions were derived in parallel in three steps. First, the height of each region was derived using dimensions published by Krogman (6). Then, the x and y dimensions of those regions were determined assuming their growth rate to be the same as the cranium. Finally, translations were applied to avoid overlap with other head regions. The volume of the spinal region was derived assuming the same growth pattern as the brain (7), and its relative position within the neck was assumed to remain constant with age.

The eyes were derived from the volumes given by the International Commission on Radiation Protection (ICRP) (9), from measurements on MR images (10) and using the relative position of the eyes compared within the upper face region. The thyroid used in these models is the same used in the ORNL pediatric models (4,5).

The total volume of the brain follows the value given by the ICRP (9). The thickness of the cerebral cortex was derived using data from Falkner and Tanner (11). The volume of the cerebellum was chosen using data from Blinkov and Glezer (12). All the inner subregions of the brain described above were derived assuming their growth to be the same as the whole brain (7). Their positions then were determined using their relative positions within the adult

brain. The white matter is considered as the remainder tissue interior to the cranium.

The five pediatric head and brain models were incorporated into the Monte Carlo radiation transport code EGS4 (13,14). All regions were coded and, to allow for photon backscatter, the trunk region defined in the anthropomorphic models derived by Cristy and Eckerman for ORNL (5) was added as a single soft-tissue region positioned below the revised head model. On completion of all particle histories, absorbed fractions of energy and their coefficient-of-variation were calculated for each target region and for each initial particle energy following the methodology described in MIRD Pamphlet No. 15 (2). Uniformly distributed monoenergetic sources of both photons and electrons were considered. Twelve energies were simulated between 10 keV and 4 MeV. For each energy and for each source region, 10 sets of 100,000 particles were run (i.e., 1,000,000 particles).

RESULTS AND DISCUSSION

Electron Absorbed Fractions

Figure 2 shows graphs of self-absorbed fraction versus initial particle energy for four electron sources in a semilog-

TABLE 1
Volumes of Regions Defined Within New Head and Brain Models (cm³)

Head region	0	1	5	10	15	Adult
Brain (total)	371.9	838.4	1194.0	1264.4	1310.2	1467.6
Caudate nuclei	2.6	6.2	8.8	9.5	9.9	10.5
Cerebellum	21.4	83.4	122.0	125.9	130.4	139.1
Cerebral cortex	160.2	353.7	485.4	557.5	571.6	622.4
Cranial CSF	5.0	13.3	30.4	40.3	44.5	56.9
Cranium	30.9	81.1	188.3	250.2	284.5	364.6
Eyes	5.3	6.5	10.9	12.4	12.4	15.2
Head (include neck and skin)	835.8	2216.2	3068.3	3490.6	3872.4	4564.9
Lateral ventricles	5.0	12.0	17.0	18.4	19.1	20.1
Lenticular nuclei	4.7	11.4	15.9	17.5	18.5	19.4
Mandible	32.1	109.8	133.0	139.4	144.8	170.5
Neck (including the skin)	43.8	94.5	145.1	228.9	329.9	567.4
Remaining head tissues	267.9	833.1	1076.3	1271.3	1425.3	1763.2
Skin	29.9	65.5	92.1	114.7	214.8	280.1
Spinal cord	1.8	4.4	5.3	6.0	6.4	6.8
Spinal CSF	4.0	8.2	11.7	13.2	14.2	14.9
Spinal skeleton	29.3	70.5	88.1	99.3	106.5	111.8
Teeth	5.9	16.1	22.1	26.0	30.2	31.2
Thalami	4.2	9.4	13.6	14.4	15.0	15.7
Third ventricle	0.3	0.7	1.1	1.1	1.2	1.2
Thyroid	1.2	1.7	3.3	7.6	11.9	19.9
Upper face region	46.7	155.6	187.4	226.2	246.2	265.5
White matter*	173.5	361.6	530.2	520.1	544.5	639.2

*Unlike all brain subregions, white matter is determined as a volume difference between total brain and other delineated subregions. A 2% decrease in white matter volume can be noted between 5- and 10-y mathematical models. This decrease is not real but is due to the restriction inherent in constructing geometric model.

CSF = cerebrospinal fluid.

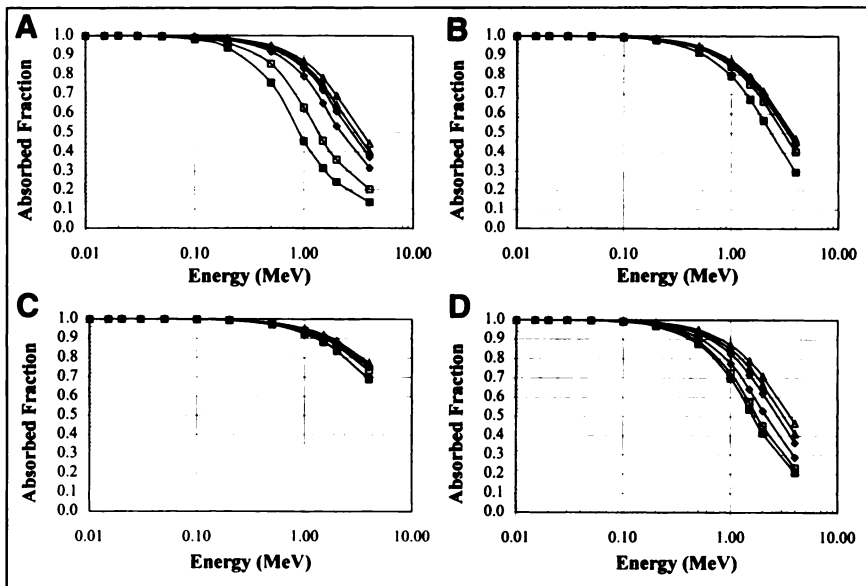


FIGURE 2. Self-absorbed fractions for electron sources within cranium (A), lentiform nuclei (B), white matter (C) and thyroid (D). Six models are shown: adult (Δ), 15 y old (\blacktriangle), 10 y old (\diamond), 5 y old (\blacklozenge), 1 y old (\square) and newborn (\blacksquare).

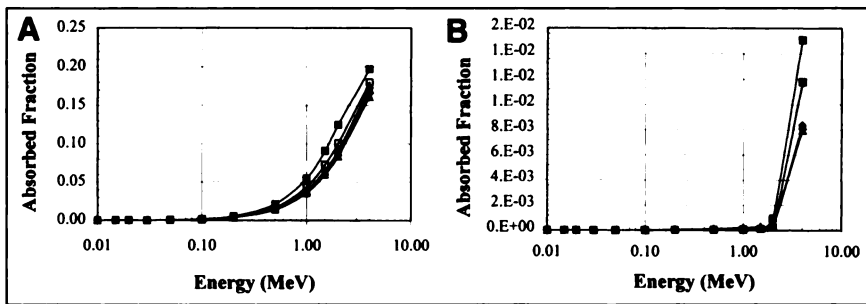


FIGURE 3. Cross-absorbed fractions for electron source in white matter, irradiating the following targets: cerebral cortex (A) and cranium (B). Six models are shown: adult (Δ), 15 y old (\blacktriangle), 10 y old (\diamond), 5 y old (\blacklozenge), 1 y old (\square) and newborn (\blacksquare).

rhythmic scale. For all ages, the self-absorbed fraction is unity at electron energies less than 100 keV. The self-absorbed fraction then decreases at higher initial electron energies. This decrease is more abrupt for smaller head regions, such as the thyroid in the newborn (Fig. 2D) than for larger head regions, such as the white matter region in the adult (Fig. 2C). For each of the graphs in Figure 2, the self-absorbed fraction curves are in order of increasing age and follow the corresponding increase of region volume with age. The largest variation with energy is seen when the source is the cranium (Fig. 2A). This is the result of the ellipsoidal shell construction of the cranium (thickness varying from 0.12 cm in the newborn to 0.53 cm in the adult). With such a regional shape, particle escape is greater than with a full region, such as the white matter. The smallest age variation of the

self-absorbed fraction is seen, therefore, when the white matter or the lentiform nuclei are source regions (Figs. 2B and C). When the source is the thyroid (Fig. 2D), large variations of the self-absorbed fractions with age are also observed as the result of larger changes in the volume of the thyroid from birth to adulthood (1.2 cm³ in the newborn and 19.9 cm³ in the adult).

Figure 3 shows graphs of the absorbed fractions of energy for electron sources in the white matter for two different targets. One of the targets is directly adjacent to the source and is the cerebral cortex within the brain. The other is the cranium, separated from the white matter by the cerebral cortex and the cranial CSF. For both targets, the absorbed fraction begins at zero. At low energies, the ranges of the electrons are too short to deposit energy in the surrounding

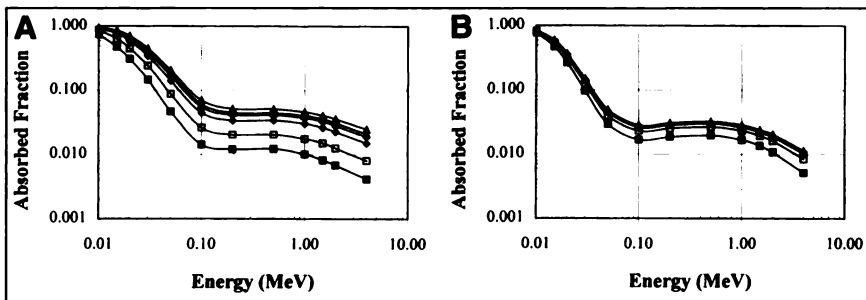


FIGURE 4. Self-absorbed fractions for photon sources within cranium (A) and lentiform nuclei (B). Six models are shown: adult (Δ), 15 y old (\blacktriangle), 10 y old (\diamond), 5 y old (\blacklozenge), 1 y old (\square) and newborn (\blacksquare).

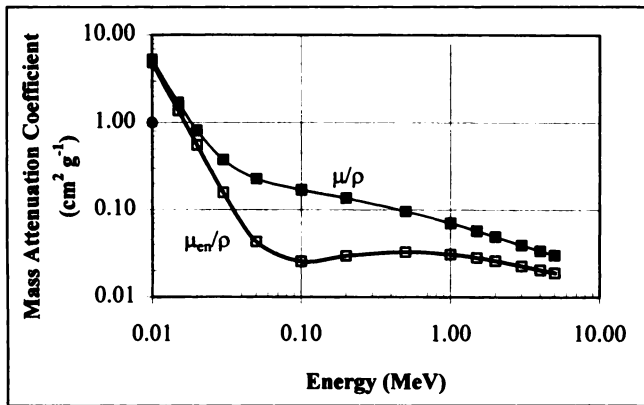


FIGURE 5. Graph of photon mass attenuation coefficients, μ/ρ , and mass energy-absorption coefficients, μ_{en}/ρ , for tissue.

target regions, and thus all the energy is deposited in the source region. As the initial electron energy increases, the electron range increases, and more energy is deposited within the surrounding regions. Small variations in the absorbed fraction with age are seen for the target within the brain (Fig. 3A). In this case, the target is directly adjacent to the white matter source and is large enough so that once an electron reaches it, the electron does not escape and deposits all its remaining energy within that region. Consequently, for a target region directly adjacent to a source region, the absorbed fraction to the target will be a function of the surface that this target has in common with the source.

On the other hand, for a nonadjacent target, such as the cranium (Fig. 3B), larger variations of the absorbed fraction with age are seen. In this case, electrons must go through the cerebral cortex and the cranial CSF before reaching the cranium, which corresponds to a total thickness of 0.64 cm in the newborn model and 1.09 cm in the adult model. The absorbed fraction, therefore, will be a function of the source-target distance and will be close to zero until the electron range is large enough to reach the target. For targets that are too far from the source to be reached by the primary electrons, some energy from bremsstrahlung photons still will be deposited. However, this energy is generally very small and is a function of the source-to-target distance, the volume of the source and the atomic number of the target. Absorbed fractions seen from bremsstrahlung photons are on the order of 10^{-6} to 10^{-7} .

Examples of absorbed fractions for 1-MeV electrons are

as follows. The self-absorbed fraction for the newborn cranium is ~ 0.45 , for the adult cranium ~ 0.87 , for the newborn thyroid ~ 0.70 and for the adult thyroid ~ 0.87 . The cross-absorbed fractions (source and target regions are different), when the white matter is the source and the cerebral cortex is the target, are 0.05 for the newborn and 0.04 for the adult. For the same white matter source and with the lentiform nuclei as the target, the electron absorbed fraction at 1 MeV is 3×10^{-3} for both the newborn and the adult. When the cranium is the target and the white matter is the source, the absorbed fraction is 5×10^{-3} for the newborn and 2×10^{-4} for the adult. The traditional MIRD methodology for nonpenetrating radiations considers 100% of the energy to be deposited within the source region and 0% within the surrounding targets. For the brain subregions, this assumption is invalid for electron energies greater than 200 keV. As the volume of the target decreases and the initial electron energy increases, explicit consideration of electron transport becomes increasingly important in assessing accurate values of absorbed fraction.

Photon Absorbed Fractions

Figure 4 displays two graphs of self-absorbed fractions versus initial particle energy for two photon sources in a logarithmic scale. In these two graphs, the absorbed fraction decreases rapidly with increasing initial photon energy. Between 100 keV and 1 MeV, it remains approximately constant and then decreases. These variations of the self-absorbed fraction with initial photon energy follow the corresponding variations of the mass energy absorption coefficient for tissue (Fig. 5). First, as a result of photoelectric absorption, there is a sharp decrease below 100 keV. Then, above 100 keV the Compton effect is dominant, and the mass energy absorption coefficient remains nearly constant up to approximately 1 MeV, where pair production interactions start to occur. As was seen for the electrons, the self-absorbed fractions for photons are in order of increasing age (increasing volume). Greater variations with age are also seen at higher energies. The largest variations are seen for the cranium as a result of its unique shape.

Figure 6 gives photon absorbed fraction graphs when the target region is adjacent or very close to the target region. In these graphs, the source region is the white matter, and the target regions are the cerebral cortex and the cranium. The absorbed fraction initially increases with energy and reaches

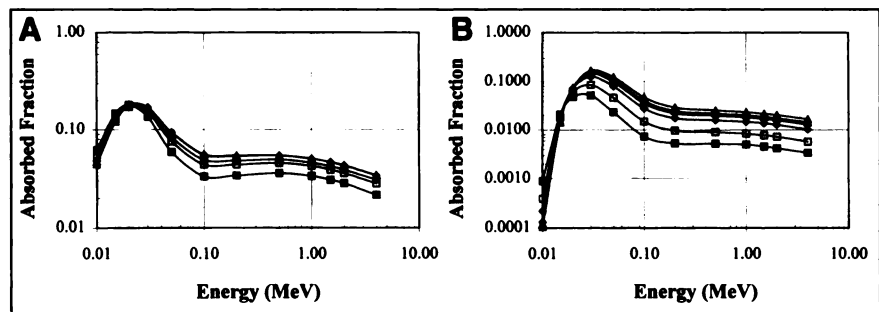


FIGURE 6. Cross-absorbed fractions for photon source in white matter and for targets include cerebral cortex (A) and cranium (B). Six models are shown: adult (Δ), 15 y old (\blacktriangle), 10 y old (\diamond), 5 y old (\blacklozenge), 1 y old (\square) and newborn (\blacksquare).

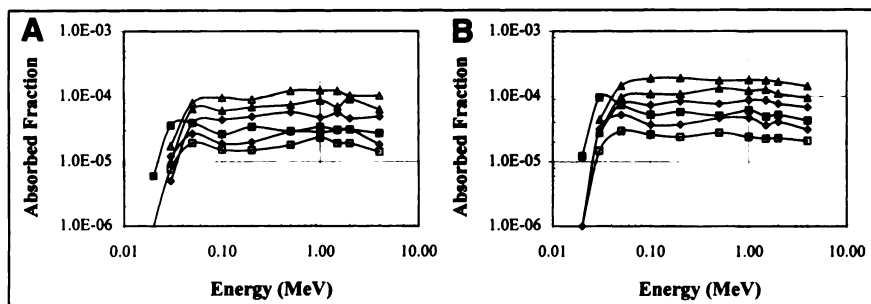


FIGURE 7. Cross-absorbed fractions to thyroid for photon source in brain (A) and lentiform nuclei (B). Six models are shown: adult (Δ), 15 y old (\blacktriangle), 10 y old (\diamond), 5 y old (\blacklozenge), 1 y old (\square) and newborn (\blacksquare).

a maximum at approximately 20–30 keV. This increase corresponds to an increase in the number of photons reaching the target, where they are fully absorbed. After reaching this maximum, the absorbed fraction follows the same trend as the mass energy absorption coefficient (Fig. 5). The dependence of the absorbed fraction with age is small for low energies. Some small variations are seen at the energy where a maximum is reached, as a result of the increase in the size of the targets. Above this maximum, larger variations are seen as a result of variations in the volume of the target regions with age. The largest age variations are again observed when the cranium is the target (Fig. 6B), because of the age dependence in the source-to-target distance.

Figure 7 shows graphs of absorbed fractions when the source and target regions are distant from each other. In these graphs, the thyroid is the target region, and the whole brain and lentiform nuclei are source regions. The absorbed fraction first increases up to a maximum at approximately 50 keV, and then remains relatively constant with increasing initial photon energy. In the same figure, the absorbed fraction is seen to vary greatly with age, reflecting the changes in both target volumes and source-to-target distances. A simple physical approximation would be to assume the absorbed fraction to follow a point-source-to-point-target attenuation and to be proportional to the volume of the target region:

$$\phi(k \leftarrow h) \approx CV_k \frac{e^{-\mu d}}{d^2}, \quad \text{Eq. 1}$$

where C is a proportionality constant, V_k is the volume of the target region, d is the source-to-target centroid distance and μ is the photon linear attenuation coefficient. In Table 2, this simple approximation is verified by comparing ratios of absorbed fraction at 4 MeV between a given pediatric head and brain model and that of the adult. The target region is the thyroid, and the source region is the brain or the lentiform nuclei. In the same table, the ratios of the expression given in Equation 1 for a given pediatric head model and the adult are also calculated, and relatively good agreement is seen. This simple verification justifies the dependence in target volume and source-to-target distance expressed in Equation 1. For both electrons and photons, variations of the absorbed fraction with energy and with age are summarized in Table 3.

Calculation of S Values

The mean absorbed dose to the target region per unit cumulated activity in the source region (S value) has been

calculated for ^{99m}Tc , for 12 source regions within the head and brain and 15 target regions and for all ages. Results are given in table form in Appendix A. In these calculations, the radionuclide decay data files of Eckerman et al. (15,16) have been used, with the β -particle and positron energy spectra finely divided into logarithmic intervals. The absorbed fractions for photon sources are used for all photon radiation components of the decay scheme. For all ages, the S values for self-irradiation of both the whole brain and the thyroid are in agreement with the S values given by the MIRDOSE3 computer code (17). This agreement is expected, because the whole brain and the thyroid have identical volumes in both of our models and in the ORNL pediatric phantoms (4,5).

Explicit Treatment of Positron Transport

A variety of positron-emitting radionuclides are used in brain imaging in conjunction with PET. Current MIRD methods for calculating absorbed fractions for positron emitters consider separately the contributions by the positron and its associated annihilation photons (18). First, the positron is assumed to deposit its initial kinetic energy totally within the source region with no particle escape (nonpenetrating radiation). Second, all positron annihilations are assumed to occur at rest, yielding two 0.511-MeV photons emitted back to back in an isotropic fashion. The absorbed fraction for each annihilation photon in a given source region is assumed to equal that calculated for monoenergetic 0.511-MeV photons uniformly distributed within that source region.

TABLE 2
Ratios of Photon Absorbed Fractions at 4 MeV for Given Pediatric Head Model and Adult Head Model

Source region	Newborn	1	5	10	15	Adult
Monte Carlo						
Brain	3.7	7.2	5.5	2.1	1.6	1.0
Lentiform nuclei	3.4	6.9	4.7	2.1	1.5	1.0
Equation 1						
Brain	3.4	6.6	4.2	2.2	1.5	1.0
Lentiform nuclei	3.2	6.7	4.1	2.2	1.5	1.0

When target region is thyroid and source region the whole brain or lentiform nuclei, as given by Monte Carlo transport code and Equation 1.

TABLE 3
Summary of Variations of Absorbed Fractions with Initial Energy of Particle and with Age of Model for Photon and Electron Sources

	Figure no.	Variation of ϕ with energy	Variation of ϕ with age
Electrons			
Self	2	$\phi \approx 1$ up to 100 keV Decreases above 100 keV MIRD assumption not valid above 100–300 keV	More abrupt decrease for smaller volumes Largest variations for shell-shaped regions (such as the cranium) Smallest variations for large regions (such as the white matter)
Cross: adjacent and close targets	3	$\phi \approx 0$ up to 100 keV Increases above 100 keV MIRD assumption not valid above 100–300 keV	Small variations for adjacent targets Larger variations for nonadjacent targets (depends on distance to source) Proportional to the source surface area directly in contact with the target
Cross: distant targets		Equals zero, except at high energy due to bremsstrahlung photons	ϕ function of the target volume, the source-to-target distance and the effective atomic number of the source region
Photons			
Self	4	ϕ decreases rapidly at energies less than 100 keV Remains constant between 100 keV and 1 MeV Decreases slightly above 1 MeV Follows the same trends as μ_{en}/ρ versus photon energy	Greater variation at high energy Absorbed fractions increase with target volume Largest variations for shell-shape regions Smallest variations for full-shape regions
Cross: adjacent and close targets	6	Increases rapidly to a maximum at 20–30 keV After the maximum, follows the same trend as μ_{en}/ρ versus energy	More variations above the maximum absorbed fraction Absorbed fraction increases with target volume Larger variations for nonadjacent and close targets (depends on distance to source)
Cross: distant targets	7	Increases rapidly to a maximum at ~ 50 keV After the maximum, remains relatively constant	Large variations with age at all energies Varies proportionally to the target volume Varies as $\exp(-\mu d)/d^2$ where d is the source-target distance

If the source region dimensions are comparable with the range of the positron, and if the positron is emitted at a relatively high energy, these traditional assumptions may no longer hold true. Two additional factors might be considered. First, in small regions such as those within the current head and brain models, annihilation events can occur outside the source region (e.g., a positron emitted within the cerebral cortex might annihilate within the cranium). Second, not all positrons would annihilate at rest, and, thus, photon energies exceeding 0.511 MeV might be considered (19).

The EGS4 code allowed for the explicit transport of positrons, and the degree to which these traditional assumptions are valid could be investigated. The transport of positrons was simulated within the brain subregions of the model of the newborn. The average initial energy of the annihilation photons was first recorded. Next, the absorbed fractions of energy from the annihilation photons and from the positrons themselves were calculated independently as functions of the initial positron energy. For the calculations of these absorbed fractions, the average initial annihilation photon energy and the average total energy deposited by the positrons were used, so that both absorbed fractions summed to 100% for all head and brain regions. Figure 8A shows the average initial energy of the annihilation photons as a function of the initial positron energy. At initial positron

energies of ~ 500 keV, the average initial energy of the annihilation photons rapidly increases at energies above 1 MeV. At a positron energy of 1 MeV, the annihilation photons have an average initial energy of 521 keV. At 2 MeV, annihilation photons are created with an average initial energy of 537 keV; at 4 MeV, photons of average initial energy 583 keV are produced. Figure 8B shows the calculated self-absorbed fractions of energy from the annihilation photons for the cerebral cortex and the caudate nuclei. In the same graph, the absorbed fractions calculated using the traditional assumption of uniform 0.511-MeV photons are indicated as horizontal lines. Differences between the Monte Carlo results and those using the traditional method start to appear at positron energies greater than 1 MeV. Those relative differences are greater for the caudate nuclei, which is a smaller region than the cerebral cortex. In comparing the absorbed fraction of energy contributed by the positron particle with electrons of similar initial kinetic energy, no statistically significant differences were seen.

The S values for positron sources can be calculated considering the explicit transport of positrons and their annihilation photons. In this case, for each positron energy within the radionuclide emission spectrum, the contribution of its annihilation photons to the total S value from the source

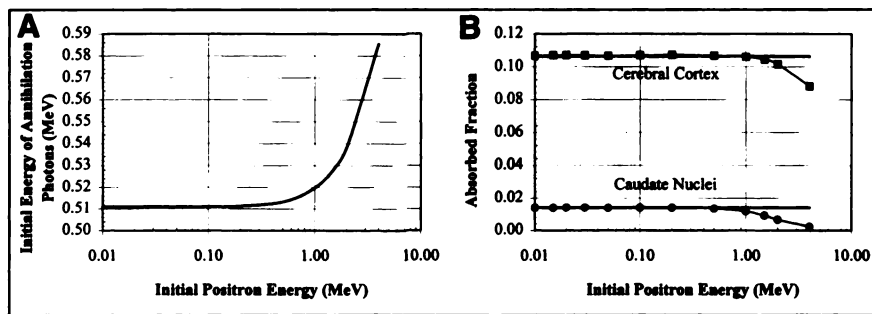


FIGURE 8. Graphs show explicit transport of positrons for newborn model for caudate nuclei (●) and cerebral cortex (■) as both source and target region. (A) Average initial energy of annihilation photons is plotted as function of initial positron energy. (B) Fraction of energy deposited by annihilation photons within positron source is plotted, and absorbed fraction for uniform source of 0.511-MeV photons is shown as horizontal lines.

region h to the target region k must also be calculated:

$$S(k \leftarrow h) = \sum_i [S_{\text{annih},E_{0i}}(k \leftarrow h) + S_{\text{pos},E_{0i}}(k \leftarrow h)], \quad \text{Eq. 2}$$

with

$$S_{\text{annih},E_{0i}}(k \leftarrow h) = \sum_i [n_i E_{\text{annih}}(E_{0i}) \Phi_{\text{annih},E_{0i}}(k \leftarrow h)], \quad \text{Eq. 3}$$

and

$$S_{\text{pos},E_{0i}}(k \leftarrow h) = \sum_i [n_i E_{\text{pos}}(E_{0i}) \Phi_{\text{pos},E_{0i}}(k \leftarrow h)]. \quad \text{Eq. 4}$$

In these equations, n_i represents the number of positrons of energy E_{0i} emitted per nuclear transition i ; $E_{\text{annih}}(E_{0i})$ is the average initial energy of the annihilation photons from positron of initial energy E_{0i} , $E_{\text{pos}}(E_{0i}) = E_{0i} - (E_{\text{annih}}(E_{0i}) - m_e c^2)$ is the average total kinetic energy deposited by the positron of energy E_{0i} ; $\Phi_{\text{annih},E_{0i}}$ is the annihilation photon specific absorbed fraction from positrons of initial energy E_{0i} ; and $\Phi_{\text{pos},E_{0i}}$ is the specific absorbed fraction for the positrons of initial energy E_{0i} .

Table 4 gives the average and maximum energy of 10 positron-emitting radionuclides used in brain nuclear medicine studies. This table also compares the S values calculated with explicit consideration of positron transport with

that calculated under the traditional assumption of a uniform 0.511-MeV photon source with electron transport. Two source and four target regions are considered. The ratios between the two calculated S values are given for all 10 radionuclides. There are almost no differences, except at high positron energies for ^{57}Cu , where differences of 5%–14% are seen for several source-target combinations. One may conclude then, that, for positron emitters with relatively low average energies, S value calculations may be accurately performed with the traditional assumption of a uniform source of electrons and with a uniform source of 0.511-MeV photons.

CONCLUSION

Five new pediatric head and brain models have been developed based on the newly adopted adult MIRSDosimetric model of the head and brain. A full set of six models with a newborn, 1, 5, 10, 15 y old and an adult is now available for suborgan head and brain dosimetry. These models include new regional source and target structures within the brain that are necessary to support the suborgan brain dosimetry of current and developing neuroimaging agents. Improvements include the incorporation of eyes, a more detailed facial skeleton and a separate neck region. These head and brain series will allow more precise dosimetry to be performed for pediatric patient studies.

TABLE 4
Comparison of S Values for Positron Emitters

	^{18}F	^{11}C	^{13}N	^{15}O	^{124}I	^{76}Br	^{62}Cu	^{122}I	^{82}Rb	^{57}Cu
E_{avg} (MeV)	0.25	0.39	0.49	0.74	0.82	1.17	1.31	1.37	1.47	3.6
E_{max} (MeV)	0.60	0.90	1.10	1.60	2.00	3.60	2.80	3.00	3.20	7.5
Target (source: caudate nuclei)										
Caudate nuclei	1.00	1.00	1.00	1.00	1.00	1.00	1.00	1.00	1.00	1.04
Cerebral cortex	1.00	1.00	1.00	1.01	1.00	1.01	1.03	1.04	1.03	1.05
Cranium	1.00	1.00	1.00	1.01	1.00	1.01	1.03	1.04	1.03	1.08
Eyes	0.98	0.98	0.99	0.99	1.00	1.00	1.01	1.02	1.01	1.14
Target (source: cerebral cortex)										
Caudate nuclei	1.01	1.00	1.00	1.01	1.00	1.00	1.01	1.01	1.01	0.95
Cerebral cortex	1.00	1.00	1.00	1.00	1.00	0.99	0.99	0.99	0.99	0.99
Cranium	1.00	1.00	1.00	1.00	1.00	0.98	0.98	0.98	0.98	0.95
Eyes	1.05	1.05	1.05	1.06	1.01	1.01	1.04	1.03	1.03	1.03

Calculated from explicit consideration of the transport of positrons and annihilation photons, and from electron and photon absorbed fraction results.

Values in lower part of table are given as ratio S value (e+)/S value (e-).

APPENDIX A

Calculated S Values (mGy/MBq/s) Within Five Pediatric Head and Brain Models for ^{99m}Tc and for 12 Brain Sources

Targets	Source = caudate nuclei					Source = cerebellum				
	NB	1 yo	5 yo	10 yo	15 yo	NB	1 yo	5 yo	10 yo	15 yo
Brain (total)	1.36E-05	7.08E-06	5.38E-06	5.13E-06	5.02E-06	1.15E-05	5.92E-06	4.45E-06	4.24E-06	4.15E-06
Caudate nuclei	1.04E-03	4.60E-04	3.29E-04	3.07E-04	2.96E-04	1.67E-06	1.07E-06	8.85E-07	7.94E-07	8.38E-07
Cerebellum	1.56E-06	1.04E-06	8.75E-07	8.03E-07	8.07E-07	1.51E-04	4.39E-05	3.15E-05	3.07E-05	2.98E-05
Cerebral cortex	3.37E-06	2.01E-06	1.61E-06	1.57E-06	1.54E-06	3.57E-06	2.03E-06	1.60E-06	1.54E-06	1.53E-06
Cranium	3.28E-06	2.05E-06	1.64E-06	1.57E-06	1.53E-06	4.74E-06	2.76E-06	2.09E-06	1.96E-06	1.92E-06
Eyes	2.85E-06	1.45E-06	1.25E-06	1.12E-06	9.73E-07	4.04E-07	2.22E-07	1.78E-07	1.56E-07	1.57E-07
Lentiform nuclei	2.57E-05	1.61E-05	1.22E-05	1.15E-05	1.10E-05	1.77E-06	1.14E-06	9.70E-07	8.89E-07	8.92E-07
Mandible	2.06E-06	9.19E-07	7.70E-07	7.07E-07	6.97E-07	7.14E-07	4.12E-07	3.40E-07	3.18E-07	3.25E-07
Other tissues	1.34E-06	5.85E-07	4.54E-07	3.95E-07	3.62E-07	1.35E-06	6.89E-07	5.31E-07	4.64E-07	4.30E-07
Skin	1.30E-06	6.49E-07	4.97E-07	4.41E-07	4.00E-07	1.60E-06	7.86E-07	5.83E-07	5.11E-07	4.77E-07
Spinal column	6.79E-07	3.52E-07	2.61E-07	2.26E-07	2.08E-07	1.93E-06	9.60E-07	7.41E-07	6.34E-07	5.07E-07
Spinal skeleton	9.46E-07	5.79E-07	4.20E-07	3.69E-07	3.55E-07	2.41E-06	1.38E-06	1.08E-06	8.91E-07	7.93E-07
Thalami	1.66E-05	9.78E-06	7.61E-06	7.04E-06	7.05E-06	2.55E-06	1.74E-06	1.46E-06	1.36E-06	1.33E-06
Thyroid	6.42E-07	1.96E-07	1.48E-07	1.22E-07	1.30E-07	4.77E-07	1.94E-07	1.58E-07	1.19E-07	9.86E-08
White matter	8.48E-06	5.24E-06	4.13E-06	4.15E-06	4.05E-06	2.55E-06	1.46E-06	1.19E-06	1.12E-06	1.12E-06

Targets	Source = cerebral cortex					Source = cranial cerebrospinal				
	NB	1 yo	5 yo	10 yo	15 yo	NB	1 yo	5 yo	10 yo	15 yo
Brain (total)	1.16E-05	5.78E-06	4.33E-06	4.16E-06	4.05E-06	4.08E-06	2.18E-06	1.65E-06	1.58E-06	1.55E-06
Caudate nuclei	3.34E-06	2.02E-06	1.61E-06	1.59E-06	1.56E-06	2.67E-06	1.49E-06	1.20E-06	1.12E-06	1.13E-06
Cerebellum	3.56E-06	2.03E-06	1.62E-06	1.55E-06	1.54E-06	4.90E-06	2.40E-06	1.82E-06	1.73E-06	1.69E-06
Cerebellum cortex	2.13E-05	1.04E-05	7.85E-06	7.07E-06	6.92E-06	5.43E-06	2.73E-06	2.01E-06	1.88E-06	1.84E-06
Cranium	4.91E-06	2.90E-06	2.17E-06	2.02E-06	1.97E-06	1.39E-05	5.80E-06	3.40E-06	2.97E-06	2.82E-06
Eyes	1.61E-06	9.61E-07	8.49E-07	6.98E-07	6.44E-07	1.58E-06	9.60E-07	8.99E-07	6.97E-07	6.62E-07
Lentiform nuclei	3.47E-06	2.03E-06	1.65E-06	1.60E-06	1.59E-06	2.79E-06	1.58E-06	1.25E-06	1.23E-06	1.21E-06
Mandible	1.23E-06	6.25E-07	5.24E-07	4.90E-07	4.86E-07	1.34E-06	6.45E-07	5.45E-07	5.10E-07	5.04E-07
Other tissues	1.07E-06	5.20E-07	3.99E-07	3.50E-07	3.18E-07	1.24E-06	5.97E-07	4.59E-07	4.00E-07	3.65E-07
Skin	1.79E-06	8.90E-07	6.58E-07	5.69E-07	5.12E-07	2.28E-06	1.08E-06	7.73E-07	6.67E-07	5.88E-07
Spinal column	9.03E-07	4.60E-07	3.52E-07	2.94E-07	2.73E-07	1.11E-06	5.69E-07	4.17E-07	3.52E-07	3.17E-07
Spinal skeleton	1.17E-06	6.67E-07	4.83E-07	4.24E-07	4.02E-07	1.32E-06	7.77E-07	5.69E-07	4.94E-07	4.61E-07
Thalami	3.52E-06	2.08E-06	1.67E-06	1.63E-06	1.59E-06	2.75E-06	1.55E-06	1.22E-06	1.20E-06	1.17E-06
Thyroid	4.42E-07	1.53E-07	1.18E-07	1.06E-07	1.00E-07	4.64E-07	1.85E-07	1.43E-07	1.15E-07	9.39E-08
White matter	4.29E-06	2.52E-06	2.03E-06	1.97E-06	1.92E-06	2.89E-06	1.68E-06	1.34E-06	1.29E-06	1.27E-06

Targets	Source = lateral ventricles					Source = lentiform nuclei				
	NB	1 yo	5 yo	10 yo	15 yo	NB	1 yo	5 yo	10 yo	15 yo
Brain (total)	1.42E-05	7.33E-06	5.60E-06	5.36E-06	5.23E-06	1.33E-05	6.95E-06	5.27E-06	5.03E-06	4.89E-06
Caudate nuclei	1.63E-05	1.02E-05	8.35E-06	7.72E-06	7.70E-06	2.59E-05	1.62E-05	1.23E-05	1.15E-05	1.11E-05
Cerebellum	2.66E-06	1.73E-06	1.43E-06	1.34E-06	1.32E-06	1.82E-06	1.12E-06	9.44E-07	8.77E-07	8.82E-07
Cerebral cortex	4.00E-06	2.45E-06	1.97E-06	1.90E-06	1.87E-06	3.50E-06	2.04E-06	1.61E-06	1.59E-06	1.57E-06
Cranium	3.03E-06	1.97E-06	1.57E-06	1.51E-06	1.49E-06	3.59E-06	2.22E-06	1.76E-06	1.67E-06	1.66E-06
Eyes	1.69E-06	8.84E-07	7.38E-07	6.17E-07	6.10E-07	2.61E-06	1.38E-06	1.18E-06	1.04E-06	9.97E-07
Lentiform nuclei	1.14E-05	6.93E-06	5.51E-06	5.27E-06	4.97E-06	6.11E-04	2.64E-04	1.93E-04	1.77E-04	1.68E-04
Mandible	1.49E-06	7.04E-07	5.80E-07	5.35E-07	5.33E-07	2.86E-06	1.27E-06	1.11E-06	1.03E-06	1.01E-06
Other tissues	1.16E-06	5.13E-07	3.97E-07	3.49E-07	3.20E-07	2.00E-06	8.16E-07	6.58E-07	5.71E-07	5.26E-07
Skin	1.26E-06	6.49E-07	4.86E-07	4.30E-07	3.93E-07	1.28E-06	6.34E-07	4.83E-07	4.24E-07	3.86E-07
Spinal column	1.01E-06	4.43E-07	3.14E-07	2.89E-07	2.67E-07	9.21E-07	4.97E-07	3.38E-07	3.13E-07	2.81E-07
Spinal skeleton	1.25E-06	6.76E-07	4.86E-07	4.21E-07	4.09E-07	1.41E-06	7.93E-07	5.87E-07	5.18E-07	5.02E-07
Thalami	1.69E-05	9.14E-06	7.40E-06	7.26E-06	6.97E-06	3.31E-05	1.68E-05	1.37E-05	1.29E-05	1.25E-05
Thyroid	5.82E-07	1.53E-07	1.39E-07	1.18E-07	1.03E-07	8.56E-07	2.81E-07	2.14E-07	2.00E-07	1.77E-07
White matter	8.83E-06	5.24E-06	4.11E-06	4.12E-06	4.02E-06	7.02E-06	4.61E-06	3.64E-06	3.61E-06	3.49E-06

APPENDIX A (Continued)

Targets	Source = spinal cerebrospinal fluid					Source = spinal skeleton				
	NB	1 yo	5 yo	10 yo	15 yo	NB	1 yo	5 yo	10 yo	15 yo
Brain (total)	1.14E-06	5.88E-07	4.43E-07	3.81E-07	3.55E-07	1.12E-06	5.74E-07	4.31E-07	3.71E-07	3.47E-07
Caudate nuclei	1.05E-06	5.24E-07	3.66E-07	3.18E-07	3.16E-07	1.03E-06	5.05E-07	3.78E-07	3.20E-07	3.15E-07
Cerebellum	1.95E-06	1.02E-06	8.12E-07	6.68E-07	5.84E-07	2.01E-06	1.01E-06	8.00E-07	6.52E-07	5.70E-07
Cerebral cortex	1.09E-06	5.43E-07	4.01E-07	3.50E-07	3.28E-07	1.06E-06	5.26E-07	3.88E-07	3.36E-07	3.19E-07
Cranium	1.73E-06	9.74E-07	7.43E-07	6.47E-07	6.05E-07	1.69E-06	9.42E-07	7.22E-07	6.22E-07	5.83E-07
Eyes	5.11E-07	2.04E-07	1.56E-07	1.26E-07	1.41E-07	5.15E-07	2.21E-07	1.45E-07	1.35E-07	1.27E-07
Lentiform nuclei	1.52E-06	6.78E-07	5.28E-07	4.62E-07	4.58E-07	1.48E-06	6.94E-07	5.06E-07	4.54E-07	4.43E-07
Mandible	1.40E-06	9.04E-07	7.06E-07	6.59E-07	7.07E-07	1.41E-06	9.06E-07	6.97E-07	6.63E-07	7.11E-07
Other tissues	3.21E-06	1.68E-06	1.37E-06	1.27E-06	1.24E-06	3.59E-06	1.84E-06	1.51E-06	1.38E-06	1.34E-06
Skin	1.27E-06	6.17E-07	4.81E-07	4.08E-07	3.66E-07	1.35E-06	6.34E-07	4.95E-07	4.20E-07	3.78E-07
Spinal column	6.86E-05	3.73E-05	3.07E-05	2.74E-05	2.59E-05	1.93E-05	1.10E-05	9.34E-06	8.42E-06	7.99E-06
Spinal skeleton	2.88E-05	1.67E-05	1.42E-05	1.27E-05	1.21E-05	1.04E-04	4.39E-05	3.62E-05	3.21E-05	3.02E-05
Thalami	1.93E-06	9.62E-07	7.43E-07	6.51E-07	5.84E-07	1.99E-06	9.26E-07	7.04E-07	6.06E-07	5.87E-07
Thyroid	4.51E-06	2.53E-06	2.37E-06	1.60E-06	1.31E-06	4.51E-06	2.61E-06	2.47E-06	1.60E-06	1.28E-06
White matter	1.06E-06	5.26E-07	3.90E-07	3.39E-07	3.22E-07	1.03E-06	5.12E-07	3.79E-07	3.34E-07	3.15E-07

Targets	Source = thalami					Source = third ventricle				
	NB	1 yo	5 yo	10 yo	15 yo	NB	1 yo	5 yo	10 yo	15 yo
Brain (total)	1.37E-05	7.15E-06	5.43E-06	5.20E-06	5.06E-06	1.39E-05	7.28E-06	5.55E-06	5.31E-06	5.18E-06
Caudate nuclei	1.66E-05	9.62E-06	7.53E-06	7.14E-06	7.06E-06	1.29E-05	7.77E-06	6.42E-06	5.91E-06	5.87E-06
Cerebellum	2.50E-06	1.73E-06	1.45E-06	1.35E-06	1.35E-06	2.59E-06	1.75E-06	1.51E-06	1.40E-06	1.39E-06
Cerebral cortex	3.44E-06	2.08E-06	1.64E-06	1.61E-06	1.58E-06	3.43E-06	2.09E-06	1.65E-06	1.62E-06	1.59E-06
Cranium	3.43E-06	2.17E-06	1.71E-06	1.64E-06	1.61E-06	3.34E-06	2.12E-06	1.67E-06	1.60E-06	1.57E-06
Eyes	1.98E-06	9.60E-07	8.26E-07	7.11E-07	6.84E-07	2.00E-06	9.43E-07	8.32E-07	7.14E-07	6.87E-07
Lentiform nuclei	3.31E-05	1.69E-05	1.36E-05	1.29E-05	1.25E-05	1.97E-05	1.05E-05	9.11E-06	8.49E-06	8.05E-06
Mandible	2.38E-06	1.15E-06	1.00E-06	9.18E-07	9.15E-07	2.30E-06	1.06E-06	9.07E-07	8.36E-07	8.21E-07
Other tissues	1.99E-06	8.83E-07	7.03E-07	6.12E-07	5.59E-07	1.90E-06	8.14E-07	6.36E-07	5.52E-07	5.08E-07
Skin	1.22E-06	6.09E-07	4.71E-07	4.11E-07	3.74E-07	1.22E-06	6.08E-07	4.70E-07	4.17E-07	3.70E-07
Spinal column	1.46E-06	6.95E-07	5.36E-07	4.50E-07	4.42E-07	1.47E-06	6.85E-07	5.13E-07	4.59E-07	4.21E-07
Spinal skeleton	1.90E-06	1.09E-06	8.21E-07	7.11E-07	6.92E-07	1.90E-06	1.05E-06	7.66E-07	6.73E-07	6.59E-07
Thalami	6.98E-04	3.24E-04	2.29E-04	2.17E-04	2.09E-04	6.51E-05	3.24E-05	2.79E-05	2.64E-05	2.46E-05
Thyroid	8.39E-07	3.38E-07	2.64E-07	2.11E-07	1.81E-07	8.45E-07	2.80E-07	2.44E-07	1.88E-07	1.68E-07
White matter	7.38E-06	4.72E-06	3.69E-06	3.70E-06	3.59E-06	8.66E-06	5.46E-06	4.21E-06	4.26E-06	4.18E-06

Targets	Source = thyroid					Source = white matter				
	NB	1 yo	5 yo	10 yo	15 yo	NB	1 yo	5 yo	10 yo	15 yo
Brain (total)	4.82E-07	1.93E-07	1.58E-07	1.26E-07	1.10E-07	1.29E-05	6.56E-06	4.95E-06	4.76E-06	4.64E-06
Caudate nuclei	5.96E-07	2.35E-07	1.71E-07	1.57E-07	1.43E-07	8.23E-06	5.21E-06	4.07E-06	4.11E-06	4.03E-06
Cerebellum	4.84E-07	1.91E-07	1.65E-07	1.25E-07	1.05E-07	2.54E-06	1.44E-06	1.17E-06	1.11E-06	1.11E-06
Cerebral cortex	4.43E-07	1.76E-07	1.43E-07	1.15E-07	1.00E-07	4.28E-06	2.49E-06	2.01E-06	1.95E-06	1.92E-06
Cranium	6.15E-07	2.83E-07	2.42E-07	1.91E-07	1.69E-07	3.57E-06	2.25E-06	1.76E-06	1.67E-06	1.65E-06
Eyes	4.22E-07	1.70E-07	1.20E-07	1.05E-07	1.01E-07	1.80E-06	1.12E-06	1.01E-06	8.23E-07	7.58E-07
Lentiform nuclei	9.53E-07	3.30E-07	2.62E-07	2.08E-07	1.96E-07	7.11E-06	4.53E-06	3.65E-06	3.61E-06	3.47E-06
Mandible	1.19E-06	9.16E-07	7.01E-07	6.33E-07	7.10E-07	1.38E-06	7.21E-07	6.04E-07	5.61E-07	5.54E-07
Other tissues	4.63E-06	2.28E-06	1.92E-06	1.65E-06	1.57E-06	1.08E-06	5.31E-07	4.11E-07	3.62E-07	3.32E-07
Skin	1.17E-06	5.06E-07	3.93E-07	3.91E-07	3.66E-07	1.48E-06	7.28E-07	5.56E-07	4.82E-07	4.47E-07
Spinal column	4.30E-06	2.38E-06	2.32E-06	1.54E-06	1.26E-06	8.65E-07	4.32E-07	3.07E-07	2.78E-07	2.82E-07
Spinal skeleton	5.84E-06	3.46E-06	3.32E-06	2.26E-06	1.91E-06	1.09E-06	6.29E-07	4.53E-07	4.04E-07	3.91E-07
Thalami	9.41E-07	3.35E-07	2.91E-07	2.28E-07	2.09E-07	7.21E-06	4.68E-06	3.65E-06	3.70E-06	3.59E-06
Thyroid	2.19E-03	1.61E-03	8.53E-04	3.88E-04	2.56E-04	4.05E-07	1.69E-07	1.58E-07	1.17E-07	1.02E-07
White matter	4.92E-07	2.02E-07	1.63E-07	1.31E-07	1.15E-07	2.27E-05	1.20E-05	8.65E-06	8.77E-06	8.47E-06

NB = newborn; yo = year old.

ACKNOWLEDGMENT

This work was supported in part by U.S. Department of Energy Grant DE-FG05-95ER62006 with the University of Florida, Gainesville, FL.

REFERENCES

1. Bouchet LG. *An Improved Dosimetric Model of the Head and Brain* [master's thesis]. College Station, TX: Texas A & M University; 1995.
2. Bouchet LG, Bolch WE, Weber DA, Atkins HL, Poston JW Sr. MIRD Pamphlet No. 15: radionuclide S values in a revised dosimetric model of the adult head and brain. *J Nucl Med.* 1999;40:63S-101S.
3. Mozley PD, Kim H-J, Gur RC, et al. Iodine-123-IPT SPECT imaging of CNS dopamine transporters: nonlinear effects of normal aging on striatal uptake values. *J Nucl Med.* 1996;37:1965-1970.
4. Cristy M. *Mathematical Phantoms Representing Children of Various Ages for Use in Estimates of Internal Dose.* ORNL/NUREG/TM-367. Oak Ridge, TN: Oak Ridge National Laboratory; 1980.
5. Cristy M, Eckerman KF. *Specific Absorbed Fractions of Energy at Various Ages from Internal Photon Sources.* ORNL/TM-8381. Oak Ridge, TN: Oak Ridge National Laboratory; 1987.
6. Krogman WM. *Growth of Man. Tabulae Biologicae.* Vol 20. Den Haag, Germany: W. Junk Publishers, Inc.; 1941.
7. Harris JA, Jackson CM, Paterson DG, Scammon RE. *The Measurement of Man.* Minneapolis, MN: University of Minnesota Press; 1930.
8. Southwood WFW. A synopsis of craniofacial growth. *Plast Reconstr Surg.* 1955;15:423-429.
9. International Commission on Radiological Protection. *Report on the Task Group on Reference Man.* ICRP Publication 23. Elmsford, NY: International Commission on Radiological Protection; 1975.
10. Salomon G, Raynaud C, Regis J, Rumeau C. *Magnetic Resonance Imaging of the Pediatric Brain: An Anatomical Atlas.* New York, NY: Raven Press; 1990.
11. Falkner FT, Tanner JM. *The Human Growth.* New York, NY: Plenum Press; 1978.
12. Blinkov SM, Glezer II. *The Human Brain in Figures and Tables.* New York, NY: Plenum Press; 1968.
13. Ford RL, Nelson WR. *The EGS Code System: Computer Programs for Monte Carlo Simulation of Electromagnetic Cascade Shower.* SLAC Report 210. Palo Alto, CA: Stanford Linear Accelerator Center; 1978.
14. Nelson WR, Hirayama RH, Rogers DWO. *The EGS4 Code System.* SLAC Report 265. Palo Alto, CA: Stanford Linear Accelerator Center; 1985.
15. Eckerman KF, Westfall RJ, Ryman JC, Cristy M. Availability of nuclear decay data in electronic form, including beta spectra not previously published. *Health Phys.* 1994;67:338-345.
16. Eckerman KF, Westfall RJ, Ryman JC, Cristy M. *Nuclear Decay Data Files of the Dosimetry Research Group.* ORNL/TM-12350. Oak Ridge, TN: Oak Ridge National Laboratory; 1993.
17. Stabin MG. MIRDose: personal computer software for internal dose assessment in nuclear medicine. *J Nucl Med.* 1996;37:538-546.
18. Snyder WS, Ford MR, Warner GG, Watson SB. *S— Absorbed Dose per Unit Cumulated Activity for Selected Radionuclides and Organs.* MIRD Pamphlet No. 11. New York, NY: Society of Nuclear Medicine; 1975.
19. Heitler W. *The Quantum Theory of Radiation.* 3rd ed. Oxford, UK: Clarendon Press; 1954.